



# Influence of the Gas Diffusion Layer Compression on the Oxygen Transport in PEM Fuel Cells at High Water Saturation Levels

Christoph Simon,<sup>\*,z</sup> Frédéric Hasché,<sup>\*</sup> and Hubert A. Gasteiger<sup>\*\*</sup>

Chair of Technical Electrochemistry, Department of Chemistry and Catalysis Research Center, Technical University of Munich, D-85748 Garching, Germany

The impact of the gas diffusion layer (GDL) compression on the oxygen transport is investigated in single cell assemblies at 50°C,  $RH = 77\%$ , 200 kPa<sub>abs</sub> and under differential flow conditions. For this, the oxygen transport resistance at low and high current densities is determined by limiting current density measurements at various oxygen concentrations for GDLs with and without microporous layer (MPL). At small current densities ( $\leq 0.4 \text{ A cm}^{-2}$ ), where no liquid water in the GDL/MPL is present, a linear increase of oxygen transport resistance with GDL compression is observed, with the GDL without MPL exhibiting a significantly lower transport resistance. For low compressions of  $\approx 8\%$ , we find that the oxygen transport resistance for the GDL with MPL is increasing disproportionately high in the high current density region ( $> 1.5 \text{ A cm}^{-2}$ ), where water condensation in the porous media takes place. A similar trend is observed for a GDL without MPL at a typical compression of 22%. Based on these results, we hypothesize that a developing liquid water film is hindering the oxygen diffusion at the interface between MPL and cathode, analogous to what is known to be formed on the cathode surface for GDLs without MPL.

© The Author(s) 2017. Published by ECS. This is an open access article distributed under the terms of the Creative Commons Attribution 4.0 License (CC BY, <http://creativecommons.org/licenses/by/4.0/>), which permits unrestricted reuse of the work in any medium, provided the original work is properly cited. [DOI: 10.1149/2.0691706jes] All rights reserved.



Manuscript submitted January 19, 2017; revised manuscript received March 14, 2017. Published March 28, 2017. This was Paper 1549 presented at the Phoenix, Arizona, Meeting of the Society, October 11–15, 2015.

The gas diffusion layer (GDL) is a key component of polymer electrolyte membrane fuel cells (PEMFCs). It is sandwiched between flow field and electrode and its function is to supply reactant gases to the electrodes, to remove product water as well as to provide good electrical and thermal contact.<sup>1,2</sup> Typically, the GDL consists of a hydrophobically treated carbon fiber paper including a microporous layer (MPL) facing the electrodes. At high current densities, the formation of liquid water inside the GDL can substantially reduce oxygen transport to the cathode and cause a significant voltage drop due to mass transport limitations.<sup>3–5</sup> Thus, the overall fuel cell performance decreases significantly.<sup>5,6</sup> To mitigate this behavior and to allow an operation at high current densities, a microporous layer coated on the GDL and facing the electrode surface is commonly used. The MPL substantially reduces the impact of water condensation by providing a uniform contact between the layers (GDL/MPL/electrode). Hence, liquid water accumulation does not occur in the vicinity of the electrode surface but rather inside the carbon fibers after passing the MPL.<sup>5,7,8</sup> Several high-resolution X-ray tomography studies have shown that liquid water transport through the MPL occurs preferably via open pathways provided by cracks in the MPL.<sup>9–11</sup> This mechanism enables the parallel transport of liquid water and oxygen, thereby minimizing the voltage drop caused by mass transport resistances. The areal crack density of a commercially available SGL MPL was found to vary between 3% and 9%,<sup>12</sup> but is very much dependent on the specific MPL properties. Furthermore, the interfacial region between MPL and catalyst layer can have a significant impact on the transport properties. X-ray imaging shows the presence of gaps between the two layers depending on the surface roughness of MPL and catalyst layer and the compression force applied.<sup>13</sup> Modeling studies demonstrate that a poor contact due to interfacial gaps can cause an increased ohmic contact resistances,<sup>14–16</sup> but the gaps can also serve as liquid water reservoir hindering the transport of oxygen.<sup>14,17</sup>

Typically, diffusion media are compressed between the flow field land areas by  $\approx 20\%$  to 25% based on their initial thickness, which corresponds to a contact pressure in the region of 1 to 2 MPa, depending on the individual mechanical properties of the GDL. On the one hand, high contact pressure reduces the electrical and thermal bulk as well as contact resistances between flow field land, GDL, and

electrode interfaces.<sup>1,18–21</sup> On the other hand the resulting high compression reduces the GDL and MPL porosity. This in turn results in a lower effective diffusivity and a higher oxygen transport resistance at dry conditions.<sup>22–26</sup> Thus, there exists an optimum compression, taking into account the electrical and mass transport losses.<sup>27,28</sup> Additionally, in a fuel cell assembly the influence of the land and channel geometry has to be taken into account, which creates a heterogeneity of material properties. The GDL compression and contact pressure in the area of the channels were shown to be significantly lower compared to the land region, which causes a higher contact resistance between MPL and electrode as well as a higher porosity in the vicinity of the channels.<sup>29–31</sup>

An experimental method to quantify the mass transport resistance of oxygen is the measurement of limiting current densities for various oxygen concentrations. Based on these measurements, Baker et al. developed a technique to separate the impact of flow field channels, GDL, MPL as well as other sources and presented a model to extract effective diffusion coefficients at the so-called dry conditions at low current densities.<sup>23</sup> There exist several studies that utilized this approach to quantify the influence of different GDL materials, MPLs, catalyst loadings, and operating conditions on the oxygen transport resistance on the cathode side.<sup>3,4,32–37</sup> It was shown that material properties like substrate type (paper, non-woven, etc.) and particularly thermal conductivity of the GDL have a significant influence on the effective diffusion and the formation of liquid water, which appears as an increase in oxygen transport resistance from a low plateau at dry conditions (i.e., absence of liquid water in GDL/MPL) to a higher plateau at wet conditions (i.e., at high water saturation levels in GDL/MPL).<sup>3</sup> This view of a transition from absence of water to high water saturation in the GDL/MPL with increasing current density was proven by Owejan et al. by comparing the local water saturation in the GDL extracted from neutron imaging in an operating fuel cell with limiting current density measurements. For this they determined the exponent of a modified Bruggeman equation for two different GDL materials.<sup>33</sup> In addition, it was shown that the flow field land-to-channel ratio has a significant impact on the diffusion limitation of a fuel cell. Shorter diffusion pathways and a more homogeneous current density distribution seem to enhance the oxygen transport for smaller lands.<sup>34</sup> Furthermore, the transport resistance in the electrode with various platinum loadings was investigated.<sup>32,34,36,37</sup>

In this paper we will use the differential cell approach to analyze the influence of the gas diffusion layer compression on the oxygen transport. Single cells with different applied GDL compressions ranging

<sup>\*</sup>Electrochemical Society Student Member.

<sup>\*\*</sup>Electrochemical Society Fellow.

<sup>z</sup>E-mail: christoph.simon@tum.de

from 8% to 53% based on their initial thickness, using a commercial GDL with MPL (SGL Sigracet GDL 25BC) are evaluated by limiting current measurements. Transport resistances are extracted for low current densities, i.e., in the dry region in the absence of water in the GDL/MPL as well as under the influence of high water saturation levels at elevated current densities. To explain the behavior at small compressions, the results are compared to measurements with a GDL without MPL (SGL Sigracet GDL 25BA). To underline our findings, we will furthermore present scanning electron microscope cross-sections of the two GDLs and pressure distribution measurements in the single cell at different compressions. For the first time, mass transport resistances as function of the GDL compression at conditions of high liquid water saturation are reported and discussed.

### Experimental

**Materials.**—In this study, a commercial GDL with MPL (SGL Sigracet GDL 25BC,  $\approx 235 \pm 20 \mu\text{m}$  thick, hydrophobically treated) and without MPL (SGL Sigracet GDL 25BA,  $\approx 190 \mu\text{m}$  thick, hydrophobically treated) is used for the cathode side, while for all tests a GDL with MPL (GDL 25BC) is used on the anode. It is important to note that GDL 25BC is based on the GDL 25BA substrate, which is additionally coated with an MPL. Fuel cell tests are performed by using a Primea Mesga catalyst coated membrane (CCM, W. L. Gore & Associates A510.1/M715.18/C580.4 equipped with a gasket) with electrode loadings of  $0.4 \text{ mg}_{\text{Pt}} \text{ cm}^{-2}$  on the cathode and  $0.1 \text{ mg}_{\text{Pt}} \text{ cm}^{-2}$  on the anode. The cell is sealed by PTFE coated glass fabrics (FIBERFLON GmbH & Co. KG) with various thicknesses. The active electrode area is  $5.0 \text{ cm}^2$ , while the GDL area is  $5.8 \text{ cm}^2$  in order to prevent misalignment of GDL and CCM during cell assembly.

**Scanning electron microscopy.**—Cross-sectional images of both GDLs with and without MPL were recorded in a scanning electron microscope (SEM) model JCM-6000 (Jeol). Samples are prepared by cutting the materials with a razor blade in order to create a clean cutting edge; subsequently the materials are fixed in a cross-section sample holder. Images were taken at 5 kV acceleration voltage at 300x magnification by a secondary electron detector. In order to determine the sample thickness, material diameters for 3 representative images at 10 positions each are measured and averaged.

**Fuel cell measurement setup.**—Fuel cell polarization curves are measured in a  $5 \text{ cm}^2$  single cell setup (Fuel Cell Technologies, Inc.) with individually designed graphite flow fields (Poco Graphite, Inc.), which comprise mirror-symmetrical flow patterns for the anode and the cathode. The flow field consists of 7 parallel channels with a channel and land width of  $0.5 \text{ mm}$  and a channel depth of  $0.8 \text{ mm}$ , which are arranged in one serpentine. More details are shown in Reference 38. The cell temperature is measured by a thermocouple directly at the center of the cathode flow field block. This corresponds to a distance of  $6 \text{ mm}$  from the flow field/GDL interface, which minimizes temperature gradients between GDL and temperature measurement location.

Different values for the GDL compression are obtained by variation of the thicknesses of the gaskets on anode and cathode side, which sandwich the gasket attached to the CCM around the active area. The compression of the GDL ( $C_{\text{GDL}}$ ) is defined as the following:

$$C_{\text{GDL}} = \left( 1 - \frac{d_{\text{GDL, A}} + d_{\text{GDL, C}}}{d_{0, \text{GDL, A}} + d_{0, \text{GDL, C}}} \right) \quad [1]$$

with  $d_{0, \text{GDL, A}}$  and  $d_{0, \text{GDL, C}}$  being the initial thicknesses and  $d_{\text{GDL, A}}$  and  $d_{\text{GDL, C}}$  the compressed thicknesses of the respective anode and cathode GDLs. The compression is calculated by

$$C_{\text{GDL}} = 1 - \frac{(d_{\text{gasket, A}} + d_{\text{gasket, C}} + d_{\text{gasket, CCM}}) \cdot (1 - C_{\text{gaskets}}) - d_{\text{CCM}}}{d_{0, \text{GDL, A}} + d_{0, \text{GDL, C}}} \quad [2]$$

taking into account the sum of anode and cathode gaskets  $d_{\text{gaskets, A}}$  and  $d_{\text{gaskets, C}}$ , the gasket attached to the CCM  $d_{\text{gasket, CCM}}$ , an experimentally determined compression of the gaskets of  $C_{\text{gaskets}} = 7\%$  in the tightened

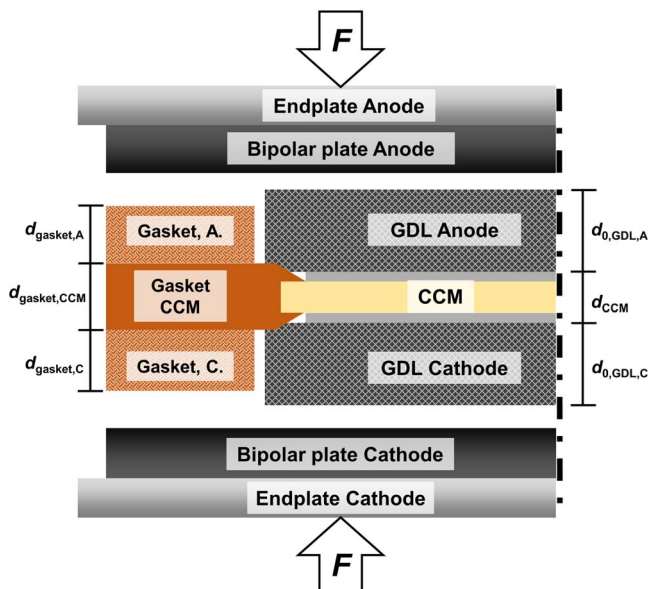


**Figure 1.** Illustration of the cell setup to clarify the calculation of the GDL compression (Eq. 2). Cell components such as GDLs, CCM, and gaskets are sandwiched between the bipolar plates and the endplates. The force ( $F$ ) in order to achieve the desired GDL compression ( $C_{\text{GDL}}$ ) is provided by 8 bolts which are tightened with a torque of  $12 \text{ Nm}$ .

cell and the thickness of the active area of the CCM  $d_{\text{CCM}}$ . Here,  $C_{\text{GDL}}$  is referring to the compression at the land area of the cell. The cell setup including all components is illustrated in Figure 1. The initial thicknesses are measured by a Mitutoyo dial gauge series 543 ( $\pm 3 \mu\text{m}$  accuracy) at five positions for the GDLs and eight positions for the gaskets for each measurement and the average is taken for the above calculation (for details see Ref. 38). The thicknesses of CCM and CCM gasket are measured by a SEM cross-section.

The CCM is sandwiched between the two GDL sheets and the flow fields. The cell endplates are tightened by eight bolts with a torque of  $12 \text{ Nm}$  in order to achieve the desired compression. The cell was connected to a custom-designed Greenlight Innovation G60 fuel cell test station equipped with an Agilent N3306A load for recording polarization curves and a Gamry Reference 3000 potentiostat for electrochemical impedance spectroscopy.

**Pressure distribution measurements.**—In order to determine the pressure distribution inside the fuel cell active area at various GDL compressions, FUJIFILM Prescale film was used in the ranges from  $0.2 \text{ MPa}$  to  $0.6 \text{ MPa}$  (ultra super low pressure range, LLLW) or from  $0.5 \text{ MPa}$  to  $2.5 \text{ MPa}$  (super low pressure range, LLW). For that, the two-sheet film was placed between flow field and GDL on the cathode side of a complete fuel cell setup (incl. CCM, gaskets, GDLs). The cell was tightened and held for  $2 \text{ min}$ ; then the pressure was released. After  $30 \text{ min}$  of color developing, the films were scanned (Epson Perfection V33) and evaluated using the provided software (Fujifilm FPD-8010E).

**Experimental procedure.**—For each GDL compression, which is listed in Table I, several individual cells were assembled and measured with  $C_{\text{GDL}}$  ranging from  $8\%$  to  $53\%$  for GDLs with MPL (GDL 25BC) and at a single compression of  $C_{\text{GDL}} = 22\%$  for GDLs without MPL (GDL 25BA) on the cathode side. Prior to fuel cell testing, each cell was conditioned by stepping the voltage under hydrogen and air at  $60^\circ\text{C}$ ,  $150 \text{ kPa}_{\text{abs}}$ , and full humidification in the following sequence:  $0.6 \text{ V}$  for  $45 \text{ min}$ ,  $0.95 \text{ V}$  for  $10 \text{ min}$ , and  $0.85 \text{ V}$  for  $5 \text{ min}$ , which was repeated for eight times. For the measurement of the limiting current density, high flow rates of  $1000 \text{ nccm H}_2$  on the anode and  $5000 \text{ nccm}$  (normal cubic centimeters per minute; volumetric flow rate

**Table I.** Average GDL compressions ( $C_{GDL}$ ) and number of individually measured cells with SGL SIGRACET GDL 25BC (with MPL) or GDL 25BA (without MPL) on the cathode side. Anode GDL: SGL SIGRACET GDL 25BC. The indicated  $\pm$ variations represent the standard deviations between the individually measured cells.

Cathode GDL type	MPL	$C_{GDL}$ [%]	Number of tested cells [-]
25BC	yes	$8 \pm 1$	4
25BC	yes	$13 \pm 2$	4
25BC	yes	$19 \pm 1$	3
25BC	yes	$23 \pm 2$	3
25BC	yes	$35 \pm 2$	3
25BC	yes	$53 \pm 1$	3
25BA	no	$22 \pm 1$	2

normalized to 273 K and 1 atm) diluted oxygen in 12 different dry mole fraction ( $x_{O_2, dry}$ ) between 0.5% and 24% on the cathode side are applied. This corresponds to high stoichiometries of  $>7$  for both reactants at all measurement conditions. The cell is adjusted to the following conditions: cell temperature of 50°C, inlet pressure ( $p_{abs}$ ) of 200 kPa, and relative humidity ( $RH$ ) of 77% (dew point of 44.8°C) on anode and cathode side. High stoichiometries and a low pressure drop of  $<15$  kPa minimize concentration and  $RH$  gradients between inlet and outlet of the flow field, enabling differential-flow conditions. For each cathode gas mixture, a polarization curve in the mass transport limited region at voltages of 0.30 V, 0.20 V, 0.15 V, 0.10 V and 0.05 V is recorded. Each voltage is held for 2 min at steady-state prior to recording the data point (average of 15 sec).

## Results

**Pressure distribution.**—In order to evaluate the pressure distribution over the active area, Figure 2b shows three examples of FUJIFILM Prescale images and Figure 2a shows the analyzed pressure applied in the channel center, land center, and on average over the active area for the various compressions. As expected, the increase of the applied pressure with compression is in agreement with the material data provided by SGL Carbon,<sup>39</sup> which is also reproduced in the appendix. It is experimentally and theoretically evident that the contact pressure in the channel center is significantly lower than in the land area, because of an absent mechanical support in the channel area.<sup>18,26,31</sup> Furthermore, imaging studies show that under compression, the diffusion medium intrudes into the flow channel, creating a variation of local GDL thickness and porosity.<sup>29,30</sup> The present measurement confirms this trend: at  $C_{GDL}$  of 20%, an average pressure of 1.1 MPa was measured, while the pressure at the land center is 1.3 MPa and 0.4 MPa at the channel center. It has been reported that the ratio between land, channel, and average pressure is a strong function of the flow field dimensions, especially of the channel width and stiffness of the GDL material.<sup>18,26,31</sup> Unfortunately, for a low compression of 8%, no differentiation between channel and land pressure is possible from the pressure distribution image: due to the stiffness of the Prescale film itself, the image shows a very homogeneous distribution of the pressure. However in a real cell setup without a mechanically stabilizing layer, the trend of a significantly lower channel pressure compared to the average pressure shown in Figure 2a is also expected at  $C_{GDL}$  of 8%.

**Scanning electron microscopy.**—Figure 3 shows representative SEM images of a GDL without MPL (a) and a GDL with MPL (b). The thicknesses of the GDL without MPL of  $\approx 156 \pm 8$   $\mu$ m (GDL 25BA) and of the GDL with MPL  $\approx 205 \pm 22$   $\mu$ m (GDL 25BC) measured by SEM equate to an approximate MPL thickness of  $\approx 49 \pm 23$   $\mu$ m. These values are reasonably similar to those measured using a dial gauge, viz.,  $\approx 153 \pm 14$   $\mu$ m for the GDLs without MPL and  $\approx 220 \pm 10$   $\mu$ m for GDLs with MPL. Here it has to be stated that the shown SEM images illustrate only a small fraction of the utilized GDL

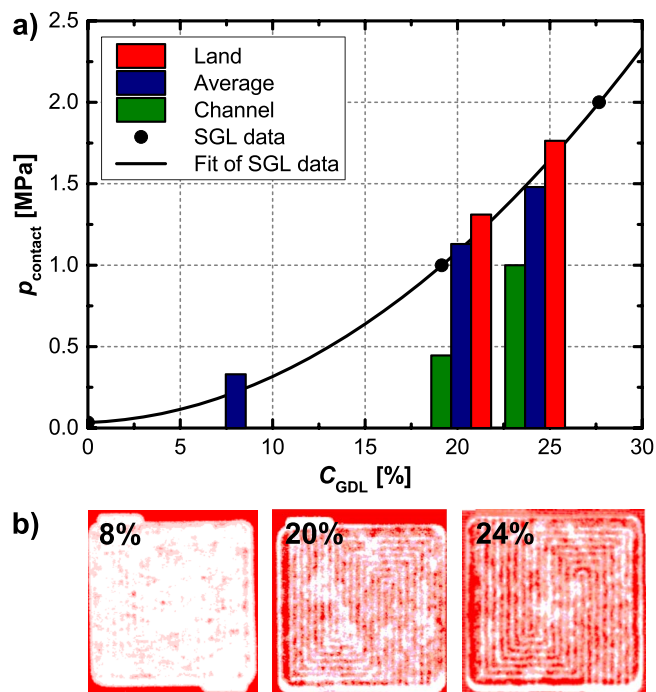


**Figure 2.** a) Measured contact pressure  $p_{contact}$  as a function of applied compression  $C_{GDL}$  for GDLs with MPL (GDL 25BC), measured with FUJIFILM Prescale. Black circles: stress-strain information from manufacturer's material data sheet<sup>39</sup> (unfortunately not available online anymore, but reproduced in the appendix). Bar diagram: average pressure in the channel center (green), the land center (red), and averaged over the entire active area (blue). FUJIFILM Prescale super low pressure range (LLW, pressure range 0.5–2.5 MPa) is used for  $C_{GDL} = 20\%$  and 24%, ultra super low pressure range (LLLW, pressure range 0.2–0.6 MPa) used for  $C_{GDL} = 8\%$ . For  $C_{GDL} = 8\%$ , the pressure on land and channel could not be separated (see text). b) Images of FUJIFILM Prescale pressure paper super low pressure range (LLW) at respective  $C_{GDL}$ .

and that even within one sample, significant variations of thickness on the order of  $\pm 10\%$  were observed. The above determined thicknesses for the GDL with and without MPL are in reasonable agreement with the manufacturer's information of  $235 \pm 20$   $\mu$ m (a similarly large standard deviation as in our SEM measurement), while above obtained thickness of the GDL without MPL is quite a bit lower than the 190  $\mu$ m specified by the manufacturer (the origin of this discrepancy is not understood).

**Limiting current measurements and data processing.**—Figure 4a shows exemplary polarization curves for two individually measured cells with different GDL compressions of 9% and 21% at three

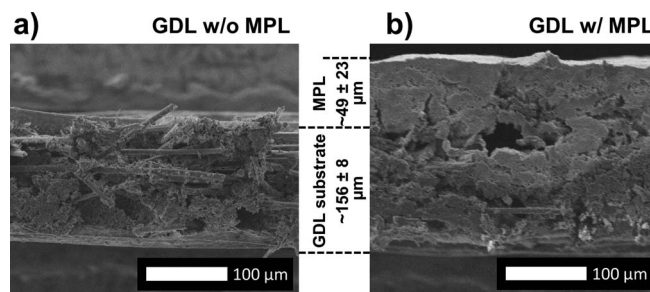


**Figure 3.** Scanning electron microscopy images of (a) GDL without MPL (GDL 25BA) and (b) with MPL (GDL 25BC). The GDL substrate thickness of  $\approx 156 \pm 8$   $\mu$ m and the thickness of the GDL with MPL of  $\approx 205 \pm 22$   $\mu$ m were extracted from SEM images (the MPL thickness indicated in the figure is estimated from the difference between (a) and (b)).



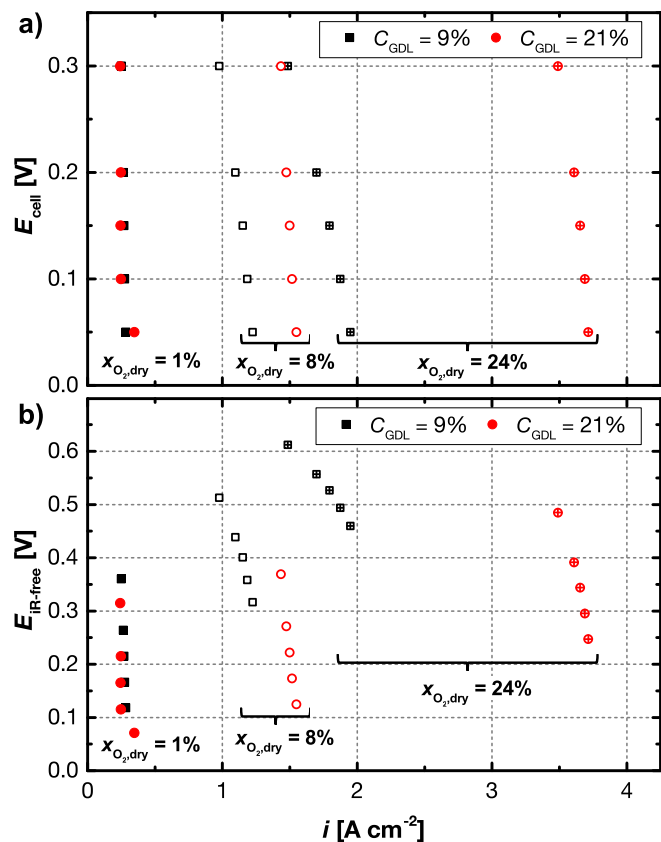


**Figure 4.** Polarization curves for three oxygen dry gas contents of  $x_{\text{O}_2, \text{dry}} = 1\%$  (full symbols),  $8\%$  (open symbols), and  $24\%$  (open, crossed symbols) for two cells with cathode GDLs with MPL (GDL 25BC) at compressions of  $C_{\text{GDL}} = 9\%$  (black squares) and  $21\%$  (red circles): a) Cell voltage ( $E_{\text{cell}}$ ); b) HFR-corrected voltage ( $E_{\text{IR-free}}$ ).

different dry mole fractions of oxygen of  $x_{\text{O}_2, \text{dry}} = 1\%$ ,  $8\%$ , and  $24\%$ . The measured geometric area normalized current densities ( $i$ ) are increasing with increasing  $x_{\text{O}_2, \text{dry}}$  due to an enhanced oxygen flux to the cathode catalyst layer. At a small dry mole fraction of  $1\%$ , the current densities at the two compressions are almost superimposed. However, at a high dry mole fraction of  $24\%$ , i.e., when large amounts of water are formed, the compression of  $21\%$  shows a significantly higher current density compared to the less compressed material. Another difference between the two compressions is the slope of the curve at  $x_{\text{O}_2, \text{dry}}$  of  $8\%$  and  $24\%$ . The polarization curve at high compressions (red symbols in Figure 4a) is almost vertical. This shape clearly indicates a mass transport limitation and excludes major influences from kinetics, proton conduction in the membrane and electrodes as well as electronic conduction resistances. In contrast, at low compressions (black symbols in Figure 4a) the curve is slightly bended. From an experimental point of view, this could be caused by high ohmic or thermal resistances as both are affected by a decrease in contact pressure.<sup>1,18,19</sup> The former is indicated by the much increased high frequency resistances (HFR) of  $150\text{--}240 \text{ m}\Omega \text{ cm}^2$  (measured at  $0.3 \text{ V}$ ) at  $C_{\text{GDL}}$  of  $9\%$ , compared to  $45\text{--}65 \text{ m}\Omega \text{ cm}^2$  for compressions of  $21\%$ . This could be either caused by an increase in contact resistance or by a higher proton resistance due to a heating of the membrane (caused by an increase in thermal resistance). In order to evaluate the HFR impact, Figure 4b shows the  $iR$ -corrected voltages of the polarization curves. Due to the higher HFR at  $C_{\text{GDL}} = 9\%$ , the  $iR$ -free voltages at this low compression are considerably higher than for  $C_{\text{GDL}} = 21\%$ , particularly at the higher current densities obtained for  $x_{\text{O}_2, \text{dry}} = 24\%$ . This might lead to the effect that a diffusion limiting current density could not be entirely reached at low compression, in which case the oxygen transport resistance would be overestimated.

The other possible explanation could be the hindered heat flux by a high thermal through-plane resistance at low compressions.<sup>19–21</sup> When the cell voltage is decreased, the fuel cell efficiency is also decreasing and more heat is released. This could result in a heating-up of the CCM, which would enhance mass transport, but could also lead to a membrane dry-out (already considered in the HFR). The temperature increase would result in a higher diffusion coefficient and lower liquid water saturation, which would cause a shift in diffusion limitation toward higher current densities, when the cell voltage is decreased. This effect would be more pronounced at low compressions as observed in the present measurement and would in contrary to above discussed ohmic resistive effects result in an underestimation of the oxygen transport resistance.

Nevertheless, the clear difference in the current density of  $\approx 1.5 \text{ A cm}^{-2}$  at  $x_{\text{O}_2, \text{dry}} = 24\%$  in Figure 4b at the same  $E_{\text{IR-free}}$  potential between  $C_{\text{GDL}}$  of  $9\%$  and  $21\%$  is indicating that the measurement is indeed dominated by oxygen transport limitations. While the ohmic resistances affect the limiting current density contrary to the thermal contact resistances at low GDL compressions and hence, might cancel each other out, we will extract the values at the same voltage for all compressions to estimate the transport resistance. This may lead to errors on the order of  $\approx 10\%$  as estimated from Figure 4b.

In summary, to extract the limiting current density ( $i_{\text{lim}}$ ), the value of  $i$  at  $0.15 \text{ V}$  was taken for  $x_{\text{O}_2, \text{dry}}$  between  $0.5\%$  and  $2\%$ , at  $0.10 \text{ V}$  between  $3\%$  and  $8\%$  and at  $0.05 \text{ V}$  between  $12\%$  and  $24\%$ . It should be noted that at low voltages and low oxygen gas content, hydrogen evolution currents become significant; hence the limiting current was extracted at  $0.15 \text{ V}$ . On the other hand, at higher oxygen concentrations and higher current densities, above mentioned effects from the electrical resistance become more significant; hence the limiting current at the lowest recorded voltage was taken into account.

The total oxygen transport resistance ( $R_T$ ) from the channels to the catalyst surface is calculated by the following equation:

$$R_T = \frac{4 \cdot F}{i_{\text{lim}}} \cdot c_{\text{O}_2} = \frac{4 \cdot F}{i_{\text{lim}}} \cdot \frac{p_{\text{abs}} - p_{\text{H}_2\text{O}}}{R \cdot T} \cdot x_{\text{O}_2, \text{dry}} \quad [3]$$

Here,  $F$  is the Faraday constant ( $96485 \text{ C mol}^{-1}$ ),  $R$  is the universal gas constant ( $8.3145 \text{ J mol}^{-1} \text{ K}^{-1}$ ),  $c_{\text{O}_2}$  is the oxygen concentration in the channel,  $T$  is the cell temperature,  $p_{\text{abs}}$  is the absolute gas pressure and  $p_{\text{H}_2\text{O}}$  is the partial pressure of water.  $R_T$  consists of the following resistances in series:<sup>3,32,36</sup>

$$R_T = R_{\text{ch}} + R_{\text{GDL}} + R_{\text{MPL}} + R_{\text{electrode}} + R_{\text{other}} \quad [4]$$

Analogous to serial electrical resistances, all single oxygen transport resistances can be summed up to a total oxygen transport resistance ( $R_T$ ).  $R_{\text{ch}}$  relates to the oxygen transport resistance originating from the transport of  $\text{O}_2$  from the bulk flow field channel to the carbon fiber material surface.  $R_{\text{GDL}}$  and  $R_{\text{MPL}}$  are referring to the resistances due to the mass transport through GDL and MPL.  $R_{\text{electrode}}$  describes the transport inside the electrode layer and the film diffusion to the catalytic active sites.  $R_{\text{other}}$  is a term for resistances from other sources and includes also interfacial resistances.

Figure 5 shows the total oxygen transport resistance  $R_T$  plotted versus the limiting current density  $i_{\text{lim}}$  for various GDL compressions. Here, the data from independent repeat experiments (s. Table I) were used to construct  $R_T$  vs.  $i_{\text{lim}}$  curves, from which then the  $R_T$  values at any given selected  $i_{\text{lim}}$  value were determined by interpolation, so that finally an average  $R_T$  value and its standard deviation over all repeat experiments could be plotted vs.  $i_{\text{lim}}$ . Significant differences in the trend of the curves are observed. Researchers at General Motors already presented data for various GDL materials with microporous layer at similar conditions for a typical compression of  $\approx 20\%$ , which is comparable to the curve for  $19\%$  and  $23\%$  in Figure 5 (green/red solid lines).<sup>3,4</sup> In general, three regions in oxygen transport (dry, transition and wet) can be discerned for GDLs with MPL, which depend on the current density. These different regions of total oxygen transport resistance are directly linked to different states of water transport through the GDL. In the dry region, at small limiting current densities ( $\lesssim 0.7 \text{ A cm}^{-2}$ ), the total oxygen transport resistance is constant at

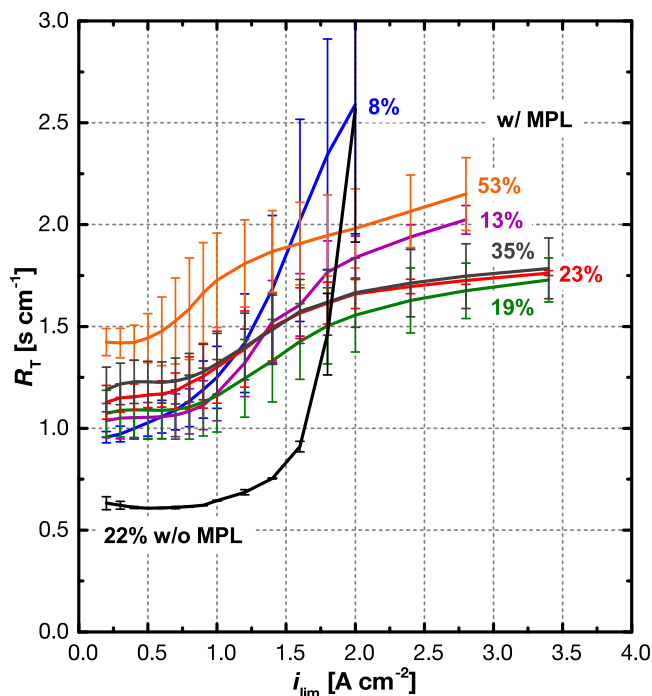


**Figure 5.** Average total oxygen transport resistance  $R_T$  calculated by Eq. 3 as a function of the limiting current density  $i_{\text{lim}}$  for cathode GDLs with MPL (GDL 25BC) and without MPL (GDL 25BA) at various compressions ( $C_{\text{GDL}}$ ) between 8% and 53%. Error bars represent the standard deviation from independent repeat experiments (the respective number of repeats are listed in Table I), which are averaged over the same current densities. Measurement conditions are  $T_{\text{cell}} = 50^\circ\text{C}$ ,  $p_{\text{abs}} = 200 \text{ kPa}$ ,  $RH = 77\%$ ; the anode GDL is always SGL 25BC.

a relatively small level ( $\approx 1.1 \text{ s cm}^{-1}$ ). Here, the GDL remains dry and the transport of water is purely driven by vapor diffusion. With increasing current density,  $R_T$  is entering a transition region, where water condensation is starting to hinder diffusion pathways of oxygen, until it reaches a reasonably constant plateau ( $\geq 2 \text{ A cm}^{-2}$ ) characterized by an  $R_T$  at an elevated level ( $\approx 1.7 \text{ s cm}^{-1}$ ). In this so-called wet region, the GDL is saturated to a maximum level with water, which causes an approximately constant total oxygen transport resistance with increasing current density. The values for  $R_T$  in the dry and wet region are in good agreement with data presented by Caulk and Baker for their unspecified material C, for which  $\approx 1.0 \text{ s cm}^{-1}$  and  $\approx 1.8 \text{ s cm}^{-1}$  were measured at the same conditions as in this study (see Figure 8 in Reference 3).

In a different article, Baker et al. showed for SGL 25BC (the same material as used in this paper) the existence of the dry, the transition, and the wet region, however measured at different operating conditions ( $T_{\text{cell}} = 65^\circ\text{C}$ ,  $p_{\text{abs}} = 310 \text{ kPa}$  and  $RH = 80\%$  compared to  $T_{\text{cell}} = 50^\circ\text{C}$ ,  $p_{\text{abs}} = 200 \text{ kPa}$  and  $RH = 77\%$ ).<sup>4</sup> Hence, the data are not directly comparable. Unfortunately, the applied compression in their study was not specified, but we assume that they used a value of  $\approx 20\%$ , as this is most typically used as standard compression by the GM group.<sup>23,36</sup> In order to compare our data with what has been measured in the literature, Figure 6 shows the comparison for two data sets from this study ( $C_{\text{GDL}} = 19\%$  and  $23\%$ , green/red solid lines) and the data for GDL 25BC (light blue solid line) from Baker et al.<sup>4</sup> Due to the different measurement conditions, the data differ significantly from each other. For a comparison, we analyze the pressure dependent part of  $R_T$  ( $\text{O}_2$  transport by molecular diffusion) in the dry region ( $\leq 0.4 \text{ A cm}^{-2}$ ), which is attributed to the diffusion medium (GDL and MPL,  $R_{\text{DM}}$ ).

$$R_{\text{DM}} = R_{\text{GDL}} + R_{\text{MPL}} \quad [5]$$

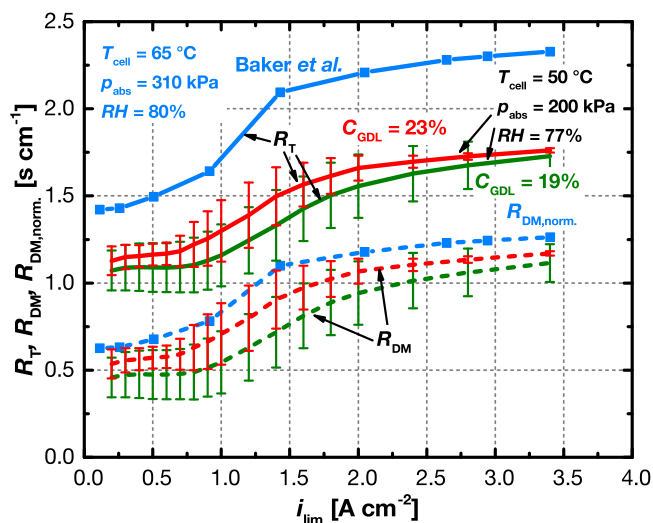


**Figure 6.** Total oxygen transport resistances ( $R_T$ , solid lines) and (normalized) diffusion medium resistances ( $R_{\text{DM}}/R_{\text{DM,norm.}}$ , dotted lines) for: GDL with MPL (GDL 25BC) at GDL compressions of 19% (green lines) and 23% (red lines) measured in our study as well as for the same GDL by Baker et al.<sup>4</sup> Data for 19% and 23% compression are taken from Figure 5 and were measured at  $T_{\text{cell}} = 50^\circ\text{C}$ ,  $p_{\text{abs}} = 200 \text{ kPa}$ ,  $RH = 77\%$ ; data from Baker et al.<sup>4</sup> were measured at  $T_{\text{cell}} = 65^\circ\text{C}$ ,  $p_{\text{abs}} = 310 \text{ kPa}$ ,  $RH = 80\%$ . In order to determine the comparable (normalized) diffusion medium resistance ( $R_{\text{DM}}/R_{\text{DM,norm.}}$ , dotted lines), Eq. 6 and Eq. 7 are applied.

Combined with Eq. 4, this results in Eq. 6. Under the assumption, that  $R_{\text{other}} \approx 0$ , because no interfacial effects are hindering oxygen transport for this compression range (explanation see later discussion), we can simplify the equation to yield:

$$R_{\text{DM}} = R_T - R_{\text{ch}} - R_{\text{electrode}} - R_{\text{other}} \approx R_T - R_{\text{ch}} - R_{\text{electrode}} \quad [6]$$

By measurements at different pressures (150 kPa, 200 kPa and 300 kPa), one can separate the pressure dependent ( $R_{\text{DM}} + R_{\text{ch}}$ ) from the pressure independent part ( $R_{\text{electrode}}$ ) of the total transport resistance.<sup>23</sup> By applying this approach, we calculate values for  $R_{\text{electrode}}$  between  $0.36 \text{ s cm}^{-1}$  and  $0.40 \text{ s cm}^{-1}$  for our data shown in Figure 5. This value is higher than what has been reported in the literature, where values of, e.g.,  $0.02$ – $0.08 \text{ s cm}^{-1}$  at  $80^\circ\text{C}$  and  $62\% RH$ ,<sup>4</sup>  $\approx 0.15 \text{ s cm}^{-1}$  at  $80^\circ\text{C}$  and  $62\%/90\% RH$ ,<sup>23,40,41</sup>  $0.2 \text{ s cm}^{-1}$  at  $80^\circ\text{C}$  and  $64$ – $80\% RH$ ,<sup>36</sup>  $0.24 \text{ s cm}^{-1}$  at  $80^\circ\text{C}$  and  $75\% RH$ <sup>35</sup> and  $0.31 \text{ s cm}^{-1}$  at  $55^\circ\text{C}$  and  $75\% RH$ <sup>35</sup> can be found for comparable cathode catalyst loadings of  $0.3$ – $0.4 \text{ mg}_{\text{Pt}} \text{ cm}^{-2}$ . The most probable reasons for the variations of  $R_{\text{electrode}}$  at the same operating temperature are different data treatment approaches, varying cell designs and individual electrode compositions and structures. Therefore, for the correction of the data by Baker et al.,<sup>4</sup> we assume the value of  $0.15 \text{ s cm}^{-1}$ , that has been reported for  $80^\circ\text{C}$  and  $62\% RH$  in their subsequent publication<sup>23</sup> using an advanced data treatment model. However it has been shown that from  $80^\circ\text{C}$  to  $65^\circ\text{C}$ ,  $R_{\text{electrode}}$  is increasing by  $\approx 25\%$  due to the temperature dependencies of Knudsen diffusion (minor) and ionomer film diffusion.<sup>35</sup> This effect is considered in the correction.

$R_{\text{ch}}$  is calculated based on a channel analysis, assuming the given flow field geometry for this study ( $0.23 \text{ s cm}^{-1}$ ) and the flow field used in Reference 23 for the literature data ( $0.33 \text{ s cm}^{-1}$ ) at the respective operating conditions. To compare the values for  $R_{\text{DM}}$  from this study and Baker et al., we normalized the literature data (condition 2:  $T_{\text{cell}} = 65^\circ\text{C}$ ,  $p_{\text{abs}} = 310 \text{ kPa}$ ,  $RH = 80\%$ ) to the conditions of this study (condition 1:  $T_{\text{cell}} = 50^\circ\text{C}$ ,  $p_{\text{abs}} = 200 \text{ kPa}$ ,  $RH = 77\%$ ) by the following relation.

$$R_{\text{DM(normalized)}} = R_{\text{DM,2}} \cdot \frac{D_{\text{OM,2}}}{D_{\text{OM,1}}} \quad [7]$$

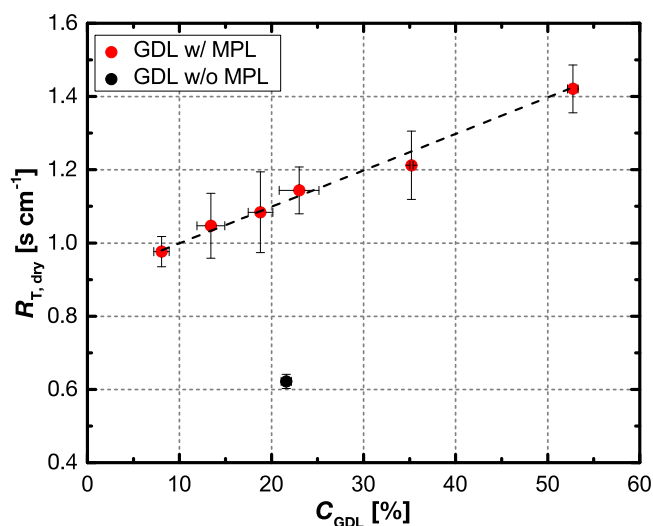


**Figure 7.** Total dry oxygen transport resistance  $R_{T,dry}$ , calculated from the average transport resistance between 0.2–0.4 A cm<sup>-2</sup> as a function of the GDL compression  $C_{GDL}$  for cathode GDL 25BC with MPL (red circle) and GDL 25BA without MPL (black circle). Values are extracted from Figure 5.

Here  $D_{OM}$  is the diffusion coefficient of oxygen in the respective gas mixture and is calculated from the binary diffusion coefficients of oxygen in nitrogen and water<sup>42</sup> and a mixture law.<sup>23</sup> Eq. 7 is valid because the same geometry factor, which is based on the channel and land widths (note that the channel and land widths in the study by Baker et al.<sup>4</sup> was also 0.5 mm), the diffusion media thickness and the ratio of in-plane to through-plane diffusion coefficient does apply.

The calculated diffusion media resistance ( $R_{DM}$ ) for compressions of 19% and 23% as well as the normalized diffusion media resistance ( $R_{DM,normalized}$ ) for the literature data is plotted in Figure 6 (dotted lines). The shapes of the curves are very similar, and the curve with 23% compression is the closest to the data by Baker et al.<sup>4</sup> In the dry region, the data from our study are 12%–25% smaller than the values from Baker et al. This can have several reasons, e.g., a higher GDL compression for their cell or an unconsidered influence of the different flow field geometries. However, due to the various assumptions made for the correction, the different cell setups, and the different measurement equipment, the agreement between the different data sets is actually quite reasonable.

**Dry region – absence of water.**—In the region of low current densities ( $\lesssim 0.7$  A cm<sup>-2</sup>), no liquid water is expected to be formed inside the cell at an  $RH$  of 77%. Hence, in this region only porosity and tortuosity of the carbon fiber material and the microporous layer determine the local diffusion of oxygen. When taking the average value of  $R_T$  between 0.2 A cm<sup>-2</sup> and 0.4 A cm<sup>-2</sup> for each adjusted compression, a total dry oxygen transport resistance ( $R_{T,dry}$ ) is determined and shown in Figure 7. This resistance  $R_{T,dry}$  should only be affected by the GDL material properties itself, its compression, and thickness besides the fixed properties of the flow field, the electrodes and the operating condition. For 19% to 23% compression, an  $R_{T,dry}$  of  $\approx 1.1$  s cm<sup>-1</sup> is measured for GDLs with MPL (GDL 25BC). This value is in good agreement with what would be expected from Baker et al. (estimated from the normalized value from Figure 6:  $R_{T,dry} \approx R_{DM,dry} + R_{electrode} + R_{ch} \approx (0.65 + 0.15 \cdot 1.25 + 0.33)$  s cm<sup>-1</sup>  $\approx 1.2$  s cm<sup>-1</sup>). For the GDL without MPL (GDL 25BA), a  $\approx 45\%$  lower  $R_{T,dry}$  of  $\approx 0.65$  s cm<sup>-1</sup> is observed, as shown in Figure 7 (black circle). This can be explained by the fact that the material without MPL is  $\approx 30\%$  thinner than the material with MPL ( $\approx 153 \pm 14$   $\mu$ m vs.  $\approx 220 \pm 10$   $\mu$ m based on our dial gauge measurements) and that the overall oxygen transport is less hindered by the material without an MPL, which acts as a series diffusion resistance with typically less

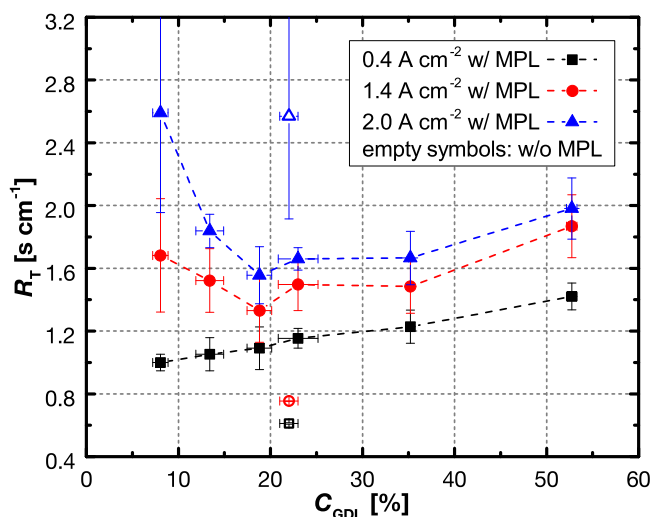


**Figure 8.** Total oxygen transport resistance  $R_T$  as function of the GDL compression ( $C_{GDL}$ ) for GDLs with MPL (GDL 25BC; filled symbols) and GDL without MPL (GDL 25BA; empty symbols), plotted for three different current densities of 0.4 A cm<sup>-2</sup> (black squares), 1.4 A cm<sup>-2</sup> (red circles), and 2.0 A cm<sup>-2</sup> (blue triangles). Values are extracted from Figure 5 at the respective current densities.

porosity and smaller pore sizes. This is indicated by air permeability measurements, which show an approximately 200 times smaller value for GDL 25BC compared to GDL 25BA.<sup>43</sup> The vapor diffusivity (which theoretically scales linearly with the oxygen diffusivity) is  $\approx 38\%$  smaller for GDL 25BC (with MPL) than for GDL 25BA (without MPL).<sup>43</sup> Normalized to the thickness (measured by dial gauge), this is resulting in a  $\approx 57\%$  smaller transport resistance for the material without MPL (GDL 25BA), which is in reasonable agreement with our findings.

For GDLs with MPL (GDL 25BC), a linear relationship between the total dry oxygen transport resistance  $R_{T,dry}$  and  $C_{GDL}$  was found, with a slope of 0.01 s cm<sup>-1</sup> per % of  $C_{GDL}$  (s. Figure 7). A similar linear relationship was found for the ratio of bulk and effective diffusion coefficient for a non-hydrophobically treated Toray 060 by limiting current density measurements.<sup>23</sup> This trend was explained by a decrease in porosity with increasing compression and was confirmed by ex-situ measurements which yielded comparable results in diffusivity and permeability.<sup>4,22,24–26</sup> The data from Baker et al.<sup>23</sup> would result in a slope for the respective recalculated values of  $R_{T,dry} \approx 0.005$  s cm<sup>-1</sup> per % of  $C_{GDL}$  (fitted between  $C_{GDL}$  of 5% and 30%, at higher compression stagnation of  $R_{T,dry}$ ), which is half of the value observed in this study and which may be related to the different microstructure of the Toray paper used by Baker et al.<sup>23</sup> compared to the GDL 25BC material used in our study (e.g., the use of untreated Toray paper vs. the hydrophobically treated GDL 25BC, differences in porosity) and the absence of an MPL for the Toray paper.

**Wet region – high water saturation levels.**—At compressions of 19%, 23%, and 35%, Figure 5 shows a reasonably flat upper plateau of  $R_T$  at  $i_{lim} > 2$  A cm<sup>-2</sup> for GDLs with MPL (GDL 25BC), as would be expected from the literature.<sup>3,4,33</sup> This, however, is not the case at lower compressions (8% and 13%), where continuously increasing  $R_T$  values with increasing limiting current density are observed. This means that for very low  $C_{GDL}$  values of 8%, the total oxygen transport resistance in the wet region is significantly higher and the limiting current densities are smaller than those obtained for conventional compressions of  $C_{GDL}$  values of  $\approx 20\%$ , even if the initial dry total oxygen transport resistance is smaller for low compressions (8% and 13%). To illustrate the  $R_T$  for different current densities as a function of compression, data from Figure 5 were replotted in Figure 8.



For the small limiting current density of  $0.4 \text{ A cm}^{-2}$ , where water transport is purely gas phase driven, an almost linear behavior between  $R_T$  and  $C_{GDL}$  is observed (see section Dry region and Figure 7). At higher limiting current densities of  $1.4 \text{ A cm}^{-2}$  and  $2.0 \text{ A cm}^{-2}$ , where the GDL is partially saturated with liquid water, the total oxygen transport resistance  $R_T$  at low compressions is increasing disproportionately compared to its behavior at higher compressions. Hence, a minimum of  $R_T$  is observed at  $C_{GDL}$  of  $\approx 19\%$ , which clearly originates purely from different oxygen transport rates. It is well known that the GDL compression has an optimum, where a maximum in fuel cell performance is achieved. So far, it has been expected that this originates mainly from a trade-off between a better mass transport at lower compressions (see section Dry region and Figure 7) and a lower electrical resistance at higher compressions, which has also been shown by fuel cell measurements with a minimum compression of  $15\%$ .<sup>27</sup> However,  $R_T$  data clearly show that this is not the only reason, because for high current densities of  $1.4 \text{ A cm}^{-2}$  and  $2.0 \text{ A cm}^{-2}$ , the smallest value for  $R_T$  is not observed at the smallest compression, but at an intermediate compression of  $19\%$ . We believe that the reason why this has not been observed previously is due to the fact that compressions far below  $15\%$  have not been examined. It is also noteworthy that for small compressions, the standard deviation for the measuring points in the wet region (expressed by the error bars in Figure 5) increase significantly due to the steep slopes of the curves. This indicates that water transport phenomena in this region are very sensitive toward compression.

The trend seen at low compressions is very similar to what is observed for GDLs without MPL (GDL 25BA), which is showing also a steep increase of  $R_T$  when water condensation is taking place (see black line in Figure 5, and open symbols in Figure 8). This is indicating that similar effects of oxygen transport hindrance by liquid water are taking place for both a GDL/MPL at low compression ( $<15\%$ ) and for a GDL without MPL at conventionally applied compression ( $\approx 20\%$ ).

### Discussion

Various in-situ X-ray or neutron tomography and radiography studies show a preferred water condensation in the vicinity of the flow field lands.<sup>8,33,44–46</sup> This is explained by better thermal contact in the land areas contacting the bipolar plate compared to the channel areas exposed to the gas convection in the flow field channels. Consequently, a cold spot between the lands and the electrode layer is formed, where water preferentially starts to condense. A transport model was proposed by Manke et al., who suggest that condensed water is eruptively transported from the land area into the flow field channels, which is confirmed by imaging the time-resolved formation, growth, and disappearance of water droplets in the vicinity of the land/channel interface.<sup>46</sup> On the other hand, Zenyuk et al. found in their X-ray computed tomography (X-ray CT) studies that water condensation occurs in the channel regions as the GDL compression is being increased from low values ( $15\%$ ) to very high values ( $35\%$  and  $47\%$ ). They explain their observation with a non-uniform porosity distribution at high compressions, which would preferably allow liquid water to be transported through the larger pores in the channel region.<sup>47</sup> Contrary to the other tomography studies, this latter work was conducted with a GDL without MPL (SGL GDL 10 BA), which could be the reason for this discrepancy; however, it should be noted that in the X-ray CT study by Deevanhxay et al.,<sup>8</sup> water formation at the cathode interface was predominantly in the land region both with and without MPL. Therefore, it is indeed likely that in the study by Zenyuk et al.,<sup>47</sup> the very high land compression resulted in an overall very poor permeability in the land regions and such a locally very low current density and water production rate.

Regarding the function of an MPL and the origin of its beneficial effect on fuel cell performance, several different hypotheses have been advanced (for a detailed summary, see Owejan et al.<sup>5</sup>). One is that the MPL might limit the number of liquid water entry points into the GDL, both in the channel and land region, thereby decreasing the local water saturation in the GDL at the point of water breakthrough.<sup>48,49</sup> An

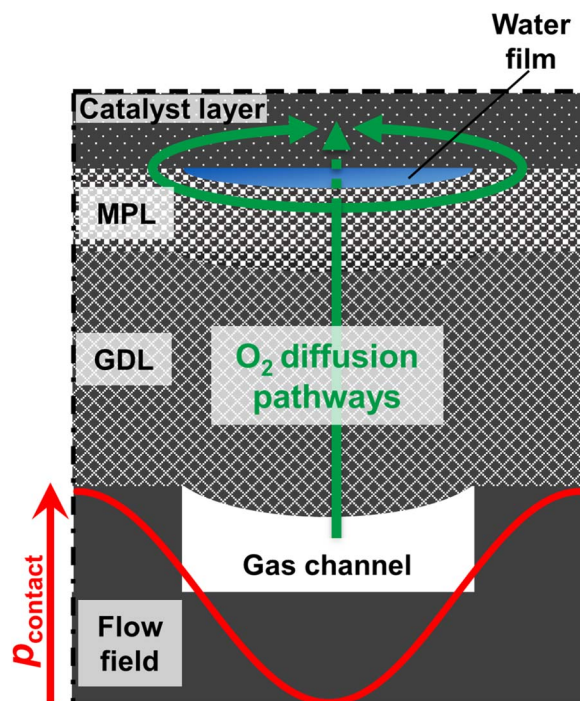


**Figure 9.** Illustration of the hypothesized water film formation at the interface of the cathode electrode layer and the MPL at low GDL compressions. Here,  $P_{\text{contact}}$  represents the contact pressure between the cathode GDL and the MEA.

alternative explanation supported by experiments with various MPL configurations is that the primary role of the cathode MPL might be to prevent the formation and/or the accumulation of liquid water at the cathode interface, suggesting that liquid water accumulation in a GDL/MPL configuration is only taking place in the larger pores of the GDL substrate, while the MPL itself would remain free of liquid water, thereby preventing the contact of liquid water formed in the large GDL pores with the catalyst layer.<sup>5</sup> We believe that it is this latter effect which causes the different behavior of the transport resistance in the presence of liquid water, when comparing GDL with and without MPL at comparable compressions of  $\approx 20\%$ , as shown in Figure 5 (s. green and red lines vs. black line). While for GDLs with MPL (GDL 25BC),  $R_T$  increases to a wet plateau which is only  $\approx 1.5$ -fold higher than the dry plateau and which is caused by reaching a partial saturation of the GDL substrate at high current densities, the GDL without MPL (GDL 25BA) is showing a steep  $\approx 4$ -fold increase of  $R_T$  without ever reaching a plateau (at least within the range of oxygen concentrations used in our study). This is consistent with the very poor low-temperature fuel cell performance without MPL shown by Owejan et al.<sup>5</sup> and with the reduced water saturation at the cathode interface in the presence of an MPL, as shown in the X-ray CT measurements by Deevanhxay et al.<sup>8</sup> as well as by Tabe et al.<sup>7</sup> by cryo-microscopy.

These findings lead us to a reasonable explanation for the increase of  $R_T$  for GDLs with MPL (GDL 25BC) at very small compressions ( $<15\%$ ). While the contact between MPL and cathode electrode layer at high compression is expected to remain very tight even in the channel region, the cathode/MPL interface in the channel regions is likely to partially separate at very low GDL compressions. This would happen preferentially in the flow field channel areas, because there the GDL is unsupported and can enter the flow field channels. Hence, the contact pressure between MPL and cathode electrode layer is only a small fraction of that under the land area as shown in Figure 2.<sup>18,26,31</sup> The pressure distribution across land and channel region is also illustrated in Figure 9. If the MPL loses its contact to the cathode electrode layer, water can accumulate on the more hydrophilic surface of the catalyst layer, which would lead to a similar effect as

that which was suggested to happen in the absence of an MPL by Owejan et al.<sup>5</sup>

Our findings show that the effect of water accumulation can be measured by varying the GDL compression. While for our flow field geometries the contact pressure in the channel center is at a reasonably high level at  $C_{\text{GDL}} = 20\%$ , this value would drop to much less than 0.3 MPa for 8% compression (i.e., much below the average compression shown in Figure 2) and below. As sketched in Figure 9, a liquid water film could be formed for these small contact pressures in the channel region, which would represent a strong diffusion barrier for the transport of oxygen to the cathode catalyst layer. Transport of gas can either occur via diffusion through this hypothesized water film or via a longer diffusion pathway through the MPL. This would cause an increase in mass transport resistance, resulting in a lower  $i_{\text{lim}}$  and a larger  $R_T$ , as is shown in Figure 6 for 8% compression; conceptually, this corresponds to an increase in the interfacial resistance contribution of  $R_{\text{other}}$  in Eq. 3. This behavior is obviously quite comparable to that of a GDL without MPL, which is showing a similar trend: i) they both have the lowest dry total oxygen transport resistances (that of the GDL without MPL is significantly smaller due to the absence of an additional diffusion barrier); ii) both show the highest values in the wet region without exhibiting a wet plateau as well as a similarly large increase of  $R_T$  between 0 and 2 A cm<sup>-2</sup>, viz.,  $\approx 2.5$ -fold for the GDL with MPL at 8% compression (s. blue line in Figure 5) and  $\approx 4$ -fold for the GDL without MPL (s. black line in Figure 5). It should be noted that a water film of only 0.02  $\mu\text{m}$  thickness ( $t_{\text{H}_2\text{O}}$ ) between the MPL and the cathode catalyst layer would result in a local oxygen transport resistance of  $R_{\text{other}} \approx 2 \text{ s cm}^{-1}$  for the operating temperature used in Figure 5 (50°C) based on the known O<sub>2</sub> solubility (Henry constant  $H_{\text{O}_2|\text{H}_2\text{O}} = 1.1 \cdot 10^{-8} \text{ Pa (mol l}^{-1})^{-1}$ ) and diffusivity in water (diffusion coefficient  $D_{\text{O}_2|\text{H}_2\text{O}} = 4.1 \cdot 10^{-9} \text{ m}^2 \text{ s}^{-1}$ ).<sup>50,51</sup> Here,  $R_{\text{other}}$  is estimated by the following equation based on the oxygen flux by Fick's diffusion ( $J_{\text{O}_2}$ ) for an applied oxygen gas concentration gradient ( $\Delta C_{\text{O}_2}$ ).

$$R_{\text{other}} = \frac{\Delta C_{\text{O}_2}}{J_{\text{O}_2}} = \frac{\frac{\Delta p_{\text{O}_2}}{R \cdot T}}{\frac{D_{\text{O}_2|\text{H}_2\text{O}}}{t_{\text{H}_2\text{O}}} \cdot \frac{\Delta p_{\text{O}_2}}{H_{\text{O}_2|\text{H}_2\text{O}}}} = \frac{t_{\text{H}_2\text{O}} \cdot H_{\text{O}_2|\text{H}_2\text{O}}}{D_{\text{O}_2|\text{H}_2\text{O}} \cdot R \cdot T} \quad [8]$$

Assuming that the water film would only be occurring in the channel region, the area averaged  $R_T$  value would be approximately half of this value for the here used channel/land ratio of 1/1 ( $\approx 1 \text{ s cm}^{-1}$ ). The estimated value is consistent with the difference between the maximum  $R_T$  value measured for a compression of 8% ( $\approx 2.6 \text{ s cm}^{-1}$ ) and the value at the comparable limiting current density for a compression of 19% ( $\approx 1.6 \text{ s cm}^{-1}$ ). This illustrates that an only 0.02  $\mu\text{m}$  thin water film in the channel region could explain our  $R_T$  measurements.

A reason why such a water film in the channel region has not yet been detected by in-situ imaging techniques with GDLs with MPL, could be that even with sophisticated measurement setups with the highest possible spatial resolutions of ca. 12  $\mu\text{m}$  for neutron imaging<sup>33</sup> and ca. 1.33–3  $\mu\text{m}$  for X-ray radiography,<sup>46,47</sup> the detection of such thin water films of on the order of 0.02  $\mu\text{m}$  would not be possible. Furthermore, when using platinum based catalysts, the very high X-ray absorption coefficient of Pt renders the detection of liquid water at the MPL/cathode layer interface very challenging.<sup>52</sup> However, in recent studies using cryo-microscopy, significant amounts of liquid water were found at the cathode MPL interface in the vicinity of the flow field channels under high-humidity conditions. Aoyama et al. investigated the effect of the preparation procedure of the MEA on liquid water formation by cryo-scanning electron microscopy.<sup>53</sup> They found significant amounts of ice at the cathode/MPL interface in the channel region after operating the fuel cell with a CCM manufactured by the decal transfer method, indicating that liquid water is accumulating in this region. In contrast to the decal transfer method, no ice was found in MEAs with gas diffusion electrodes (GDE), in which the catalyst layer is directly applied to the MPL and for which a better adhesion between electrode and MPL is expected. Based on these findings, the authors concluded that the water accumulation in case of the catalyst coated membrane is caused by a poor contact

between catalyst layer and MPL in the channel region, leading to the formation of a water film. One light microscope study focused on the effect of the microporous layer on water transport.<sup>7</sup> While for GDLs without an MPL, ice was found equally distributed among flow field channel and land areas, for GDLs equipped with an MPL, ice was preferentially found in the flow field channel regions. This suggests that the MPL can prevent water accumulation in the flow field land area, where high contact pressure is observed; at the same time, however, at the decreased contact pressure in the channel regions, liquid water can accumulate in gaps between the MPL and the cathode electrode layer.<sup>7,14,15,53</sup> Finally, this is also supported by the calculation of the water storage capacities at the cathode/MPL interface based on surface roughness measurements: Swamy et al. predict a three times higher maximum water content inside interfacial gaps without applied compression in the flow field channels compared to 1.5 MPa, which corresponds to a typical flow field land compression pressure.<sup>14</sup>

The here presented effect of high oxygen mass transport resistances at very low compressions is not only relevant in case of inhomogeneous compression of the diffusion medium, e.g., if the cells of a stack are locally under compressed. But it might also be relevant when considering to increase the flow field channel-to-land ratio in automotive fuel cells, which can result in very low contact pressures at the channel center.<sup>26,34</sup> This would be expected to facilitate the proposed water film formation even if the dry transport resistance for a high channel-to-land ratio is smaller than for narrow channels.<sup>34</sup> Likewise, a trend toward thinner GDLs could result in similar effects as observed in this study: while their advantage is an improved mass transport, their disadvantage is the concomitant decrease of the shear and bending stiffness, which results in a smaller contact pressure in the channel center. Therefore, interfacial effects between MPL and electrode layer have to be taken into account when optimizing flow field, GDL, MPL, and CCM for high performance.

## Conclusions

In conclusion, we show experimental data at  $T_{\text{cell}}$  of 50°C,  $RH$  of 77% and  $p_{\text{abs}}$  of 200 kPa which allow the determination of the total oxygen transport resistance  $R_T$  between the gas flow field channels and the cathode electrode as a function of the applied gas diffusion layer compression ( $C_{\text{GDL}}$ ) of a GDL with MPL (SGL GDL 25BC). We observe that oxygen transport in dry GDLs with MPL at small limiting current densities  $< 0.7 \text{ A cm}^{-2}$ , where transport of water is purely driven by vapor diffusion and no liquid water is expected, is hindered by an increase in compression due to a loss in GDL porosity. Hence, we measure a linear increase of  $R_T$  with increasing  $C_{\text{GDL}}$ .

For current densities  $> 1.5 \text{ A cm}^{-2}$ , where liquid water is formed, the total oxygen transport resistance  $R_T$  is increasing disproportionately for less compressed diffusion layers, i.e., for  $C_{\text{GDL}} \leq 13\%$ . We find a minimum value of  $R_T$  at GDL compressions of 19%, which solely originates from an optimum of the oxygen transport rate. Comparative measurements with a GDL without MPL (GDL 25BA) show a similar trend, viz., a significantly increasing  $R_T$  at higher current densities, which can be explained by the flooding of the GDL close to the cathode surface. For GDLs with MPL, the formation of a liquid water film as illustrated in Figure 9 at the cathode/MPL interface in the flow field channel region can rationalize this phenomenon.

## Acknowledgments

This research was carried out within the framework of the joint project "Optigaa2". Financial support by the German Federal Ministry of Economic Affairs and Energy (grant number 03ET6015E), Freudenberg Performance Materials SE & Co. KG and Daimler AG is gratefully acknowledged. We are also thankful for valuable discussions with Daniel Baker (General Motors) and David Müller (TUM).



**Table AI. Material properties of SGL GDL 25 BC reproduced from a table given in the manufacturer's information,<sup>39</sup> which is unfortunately not anymore available online.**

Properties	Units	GDL 25BC
Ash content <sup>1</sup>	%	<0.25
Areal weight <sup>2</sup>	g m <sup>-2</sup>	90 ± 10
Thickness (@ 5psi load) <sup>3</sup>	μm	235 ± 20
Thickness (@ 1 MPa load) <sup>3</sup>	μm	190 ± 20
Thickness (@ 2 MPa load) <sup>3</sup>	μm	170 ± 20
Compressibility (@ 1 MPa) <sup>4</sup>	%	ca. 19
TP El. Resistance (@ 1MPa) <sup>5</sup>	mΩ cm <sup>2</sup>	<12
IP Pressure Drop (@ 1 MPa)	bar	0.8

<sup>1</sup>DIN 51903;<sup>2</sup>SGL internal, based on DIN EN ISO 536;<sup>3</sup>SGL internal, based on DIN EN ISO 9073;<sup>4</sup>SGL internal, based on DIN 53885;<sup>5</sup>SGL internal, based on DIN 51911.

## Appendix

See Table AI.

## References

- M. F. Mathias, J. Roth, J. Fleming, and W. Lehnert, in *Handbook of Fuel Cells*, W. Vielstich, H. A. Gasteiger, and A. Lamm Editors, John Wiley & Sons, Ltd (2010).
- J. M. Morgan and R. Datta, *J. Power Sources*, **251**, 269 (2014).
- D. A. Caulk and D. R. Baker, *J. Electrochem. Soc.*, **157**, B1237 (2010).
- D. R. Baker, C. Wieser, K. C. Neyerlin, and M. W. Murphy, *ECS Transactions*, **3**, 989 (2006).
- J. P. Owejan, J. E. Owejan, W. B. Gu, T. A. Trabold, T. W. Tighe, and M. F. Mathias, *J. Electrochem. Soc.*, **157**, B1456 (2010).
- H. Li, Y. H. Tang, Z. W. Wang, Z. Shi, S. H. Wu, D. T. Song, J. L. Zhang, K. Fatih, J. J. Zhang, H. J. Wang, Z. S. Liu, R. Abouatallah, and A. Mazza, *J. Power Sources*, **178**, 103 (2008).
- Y. Tabe, Y. Aoyama, K. Kadowaki, K. Suzuki, and T. Chikahisa, *J. Power Sources*, **287**, 422 (2015).
- P. Deevanhxay, T. Sasabe, S. Tsushima, and S. Hirai, *Electrochem. Commun.*, **34**, 239 (2013).
- H. Markotter, J. Haussmann, R. Alink, C. Totzke, T. Arlt, M. Klages, H. Riesemeier, J. Scholta, D. Gerteisen, J. Banhart, and I. Manke, *Electrochem. Commun.*, **34**, 22 (2013).
- H. Markötter, I. Manke, P. Krüger, T. Arlt, J. Haussmann, M. Klages, H. Riesemeier, C. Hartnig, J. Scholta, and J. Banhart, *Electrochem. Commun.*, **13**, 1001 (2011).
- P. Deevanhxay, T. Sasabe, S. Tsushima, and S. Hirai, *J. Power Sources*, **230**, 38 (2013).
- F. E. Hizir, S. O. Ural, E. C. Kumbur, and M. M. Mench, *J. Power Sources*, **195**, 3463 (2010).
- S. Prass, S. Hasanpour, P. K. Sow, A. B. Phillion, and W. Mérida, *J. Power Sources*, **319**, 82 (2016).
- T. Swamy, E. C. Kumbur, and M. M. Mench, *J. Electrochem. Soc.*, **157**, B77 (2010).
- I. V. Zenyuk, E. C. Kumbur, and S. Litster, *J. Power Sources*, **241**, 379 (2013).
- S. Kim, M. Khandelwal, C. Chacko, and M. M. Mench, *J. Electrochem. Soc.*, **156**, B99 (2009).
- A. R. Kalidindi, R. Taspinar, S. Litster, and E. C. Kumbur, *Int. J. Hydrogen Energy*, **38**, 9297 (2013).
- J. Kleemann, F. Finsterwalder, and W. Tillmetz, *J. Power Sources*, **190**, 92 (2009).
- I. Nitta, O. Himanen, and M. Mikkola, *Fuel Cells*, **8**, 111 (2008).
- E. Sadeghi, N. Djilali, and M. Bahrami, *J. Power Sources*, **196**, 246 (2011).
- G. Karimi, X. Li, and P. Teertstra, *Electrochim. Acta*, **55**, 1619 (2010).
- P. K. Das, X. G. Li, and Z. S. Liu, *Applied Energy*, **87**, 2785 (2010).
- D. R. Baker, D. A. Caulk, K. C. Neyerlin, and M. W. Murphy, *J. Electrochem. Soc.*, **156**, B991 (2009).
- N. Zamel, X. G. Li, and J. Shen, *Energy Fuel*, **23**, 6070 (2009).
- N. Zamel, N. G. C. Astrath, X. G. Li, J. Shen, J. Q. Zhou, F. B. G. Astrath, H. J. Wang, and Z. S. Liu, *Chem. Eng. Sci.*, **65**, 931 (2010).
- I. Nitta, T. Hottinen, O. Himanen, and M. Mikkola, *J. Power Sources*, **171**, 26 (2007).
- J. Ge, A. Higier, and H. Liu, *J. Power Sources*, **159**, 922 (2006).
- M. B. Sassini, Y. Garsany, B. D. Gould, and K. Swider-Lyons, *J. Electrochem. Soc.*, **163**, F808 (2016).
- C. Totzke, G. Gaiselmann, M. Osenberg, J. Bohner, T. Arlt, H. Markotter, A. Hilger, F. Wieder, A. Kupsch, B. R. Muller, M. P. Hentschel, J. Banhart, V. Schmidt, W. Lehnert, and I. Manke, *J. Power Sources*, **253**, 123 (2014).
- N. Khajeh-Hosseini-Dalasm, T. Sasabe, T. Tokumasu, and U. Pasaogullari, *J. Power Sources*, **266**, 213 (2014).
- H. Butsch, C. Roth, D. Ritzinger, G. Hoogers, and A. Bock, *J. Electrochem. Soc.*, **159**, B709 (2012).
- T. A. Greszler, D. Caulk, and P. Sinha, *J. Electrochem. Soc.*, **159**, F831 (2012).
- J. P. Owejan, T. A. Trabold, and M. M. Mench, *Int. J. Heat Mass Transfer*, **71**, 585 (2014).
- Y. Fukuyama, T. Shiomi, T. Kotaka, and Y. Tabuchi, *Electrochim. Acta*, **117**, 367 (2014).
- Z. Lu, J. Waldecker, M. Tam, and M. Cimenti, *ECS Transactions*, **69**, 1341 (2015).
- J. P. Owejan, J. E. Owejan, and W. B. Gu, *J. Electrochem. Soc.*, **160**, F824 (2013).
- A. Kongkanand and M. F. Mathias, *The Journal of Physical Chemistry Letters*, **7**, 1127 (2016).
- C. Simon, F. Hasché, D. Müller, and H. A. Gasteiger, *ECS Transactions*, **69**, 1293 (2015).
- SIGRACET GDL - Gas Diffusion Layer non-woven fabric (booklet)*, SGL CARBON GmbH (2014), downloaded in 01/2015.
- Y. Ono, T. Mashio, S. Takaichi, A. Ohma, H. Kanesaka, and K. Shinohara, *Ecs Transactions*, **28**, 69 (2010).
- K. Sakai, K. Sato, T. Mashio, A. Ohma, K. Yamaguchi, and K. Shinohara, *Ecs Transactions*, **25**, 1193 (2009).
- R. Bird, W. Stewart, and E. Lightfoot, *Transport Phenomena (revised second ed.)*, John Wiley & Sons (2007).
- J. M. LaManna and S. G. Kandlikar, *Int. J. Hydrogen Energy*, **36**, 5021 (2011).
- I. Manke, C. Hartnig, M. Grünerbel, W. Lehnert, N. Kardjilov, A. Haibel, A. Hilger, J. Banhart, and H. Riesemeier, *Appl. Phys. Lett.*, **90**, 174105 (2007).
- T. Sasabe, S. Tsushima, S. Hirai, K. Minami, and K. Yada, *ECS Transactions*, **25**, 513 (2009).
- I. Manke, C. Hartnig, N. Kardjilov, H. Riesemeier, J. Goebbels, R. Kuhn, P. Krüger, and J. Banhart, *Fuel Cells*, **10**, 26 (2010).
- I. V. Zenyuk, D. Y. Parkinson, G. Hwang, and A. Z. Weber, *Electrochem. Commun.*, **53**, 24 (2015).
- J. T. Gostick, M. A. Ioannidis, M. W. Fowler, and M. D. Pritzker, *Electrochem. Commun.*, **11**, 576 (2009).
- Z. Lu, M. M. Daino, C. Rath, and S. G. Kandlikar, *Int. J. Hydrogen Energy*, **35**, 4222 (2010).
- T. R. Rettich, R. Battino, and E. Wilhelm, *J. Chem. Thermodyn.*, **32**, 1145 (2000).
- R. T. Ferrell and D. M. Himmelblau, *J. Chem. Eng. Data*, **12**, 111 (1967).
- C. Hartnig, I. Manke, R. Kuhn, S. Kleinau, J. Goebbels, and J. Banhart, *J. Power Sources*, **188**, 468 (2009).
- Y. Aoyama, K. Suzuki, Y. Tabe, T. Chikahisa, and T. Tanuma, *J. Electrochem. Soc.*, **163**, F359 (2016).